WIND TUNNEL TESTING OF A VARIABLE-PITCH QUADROTOR UAV ISOLATED ROTOR

Fabio Riccardi

Dipartimento di Scienze e Tecnologie Aerospaziali - Politecnico di Milano
Via La Masa 34, 20156 Milano, Italy

Abstract: This paper deals with the aerodynamics characterization of a variable-pitch quadrotor UAV isolated two-bladed teetering rotor in working conditions far beyond hover, in terms of free stream velocity incident on rotor disk and its angle of attack. The survey conducted is addressed to evaluate rotor forces, power and flapping angles behavior in forward flight (not only for trimmed conditions) and to investigate the rotor mean inflow in descent, especially in Vortex Ring State (VRS). A dedicated analytical model for the rotor aerodynamics was developed, in both above operating regimes of interest, with a level of detail and complexity suitable for flight mechanics purposes. Modeling results were validated carrying out a proper wind tunnel experimental campaign on the full scale complete rotor system of the considered UAV, minimizing test duration and equipment costs. The experimentally validated model for rotor aerodynamics was coupled with quadrotor rigid body equations of motion and adopted for control synthesis applications.

1. INTRODUCTION AND MOTIVATIONS

Quadrotors have become increasingly popular in recent years as platforms for both research and commercial small-scale Rotary-wing Unmanned Aerial Vehicle (RUAV) applications. In particular, some of the envisaged applications for quadrotors lead to tight performance requirements on the control system. This, in turn, calls for increasingly accurate dynamics models of the vehicle to which advanced controller synthesis approaches can be applied.
The problem of mathematical modeling of quadrotor dynamics has been studied extensively, see, *e.g.*,[1] and the references therein for an exhaustive state of the art review. In particular, it is apparent from the literature that models for quadrotor dynamics are easy to establish as far the kinematics and dynamics of rigid body linear and angular motion are concerned, so that a large portion of the available works dealing with quadrotor control is based on such models, adopting a rough momentum theory approach in rotor forces and moments estimation. The reason is that quadrotor mostly operates in hover or at very slow velocity during a mission and in these conditions it is absolutely reasonable to adopt assumptions resulting in strongly simplified models for rotors aerodynamics. On the other hand a quadrotor may also operate in forward flight at considerable velocity, execute aggressive maneuvers at high angular velocity and attitude angles, operate in presence of wind disturbances and perform steep descent. Characterizing rotor aerodynamics in these conditions and its effect on flight mechanics (and related control issues) of these small size vehicles is far from trivial, and the topic was faced only in few works.
In particular in[2] the effect on rotor thrust of free stream velocity and its angle of attack respect to rotor, and the blade flapping, were characterized considering a variable RPM (fixed blade pitch) quadrotor. In[3] the previous results were exploited to develop, for the same vehicle, a proper rotor aerodynamics model and relative control system in order to performing aerobatic maneuvers. In both cited cases the considered quadrotor adopts the most common rotor architecture, without articulation for blade flapping and collective pitch control (similar to a propeller, rigidly mounted to the shaft): vehicle control is obtained varying the rotors RPM and the flapping is absolved by the blades flexibility. The role of propeller flexibility in quadrotor dynamics modeling is discussed widely in[4]. While in[5] a quadrotor dynamics model was proposed, taking into account blade flapping effects for a sprung teetering rotor hub, but with variable RPM architecture.
To the best of the author knowledge the proposed rotor aerodynamics characterization in wind tunnel for forward flight and descent conditions is the first contribution considering a variable-pitch quadrotor with teetering hub: in the recent[6] the rotor aerodynamics model parameters of a fixed pitch quadrotor were identified, through wind tunnel test campaign on the entire vehicle, for hover, vertical climb and forward flight conditions.
The considered vehicle is the AERMATICA ANTEOS A2-MINI/B, showed in Figure 1, a variable-pitch quadrotor UAV for aerial work applications (MTOW of 9 kg), adopting an unconventional teetering articulation for the two-bladed rotors (main parameters resumed in Table 1), with the flapping motion not completely free but restrained by rubber elastic

Rotor angular velocity [RPM]	2000
Rotor radius [m]	0.375
Tip speed [m/s]	78.54
Blade mean geometric chord [m]	0.0406
Blade linear built-in twist [rad]	0.2517
Rotor solidity	0.069
Blade mass [kg]	0.043
Blade airfoil	NACA 3514
Brushless motor angular velocity [RPM]	10400
Motor max. continuous power [W]	350

Table 1: ANTEOS A2-MINI/B rotors parameters.

elements. The pitch command horn introduces a pitch-flap coupling through a δ_3 hinge angle of about 12°.

The paper is organized as follow. First are described the adopted analytical models for the rotor aerodynamics, in Section 2 for the forward flight condition and in Section 3 the one dedicated to descent regime. Then in Section 4 is described the conducted wind tunnel testing campaign and Section 5 show some representative results comparing the model estimates with the experimental data. Finally in Section 6 are presented some applications of the developed models to quadrotor control synthesis.

Figure 1: AERMATICA ANTEOS A2-MINI/B.

2. ANALYTICAL MODEL ADOPTED FOR FORWARD FLIGHT CONDITION

The desired rotor global performance parameters (mean induced velocity, thrust, H-force, mechanical and electrical power) and longitudinal/lateral flapping angles, were calculated as function of three independent variables (defining each wind tunnel test point), without mutual dependency imposed by vehicle trim: wind velocity, rotor angle of attack (AoA) respect to incident velocity and blade collective pitch. Accordingly it was implemented a relatively simple model, considered appropriate for desired flight mechanics purposes, based on well-known closed-form equations of Blade Element Theory (BET) in forward flight, as developed in[7] (reverse flow region ignored, root and tip losses neglected).

The experimental data from fixed point isolated rotor test are available, executed on a proper hover tower assuring no ground interference effects: thrust $C_{T_{meas}}$ and torque $C_{Q_{meas}}$ measured coefficients on test points (varying the collective pitch) are related with the rotor drag coefficient C_d through the following equation (assuming an ideal twisted blade, ideal induced losses[7]):

$$C_{Q_{meas}} = \frac{{C_{T_{meas}}}^{3/2}}{\sqrt{2}} + \frac{C_d \sigma}{8}, \quad (1)$$

where σ is the rotor solidity. Furthermore it is possible to define the average blade angle of attack[7] as:

$$\overline{\alpha} = \frac{6 C_{T_{meas}}/\sigma}{a}, \quad (2)$$

where a is the lift curve slope of rotor blades, assumed constant and equal to the 2-D value of the blade airfoil (linear region, free from stall and compressibility effect) without serious loss of accuracy in hovering. Combining Equation 1 with 2 for each hover tower test point, the rotor drag coefficient is defined as function of average blade angle of attack and applying a quadratic polynomial fitting (as showed in Figure 2) the three-term drag polar for the rotor can be defined as:

$$C_d = C_{d_0} + C_{d_1}\overline{\alpha} + C_{d_2}\overline{\alpha}^2 = 0.0215 - 0.135\overline{\alpha} + 1.85\overline{\alpha}^2. \quad (3)$$

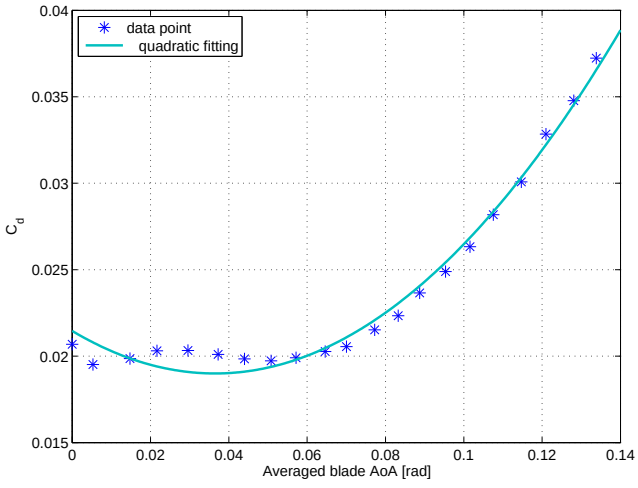

Figure 2: Rotor drag polar from fixed point isolated rotor test on hover tower.

In order to complete the input data feeding the model, it was necessary to characterize the unconventional teetering articulation. For the considered

rotor head design, the effective flapping hinge offset is replaced by an equivalent torsional spring, the effect of which is obtained by proper rubber elastic elements. Hence it was carried out an experimental measure of the equivalent flapping hinge torsional stiffness, imposing to the articulation a given moment and measuring the rotor hub flapping angle (maximum range of about $\pm 8°$) with a digital inclinometer. The results are showed in Figure 3. Clearly the non linear rubber behavior implies a cubic trend of the torsional spring moment varying the flapping angle, hence the spring stiffness is not constant and it involves the adoption of an iterative calculation to determine the flapping angles, as described further. The polynomial fitting results are reported below, relating the spring moment M_{sprg} and the flapping angle β:

$$M_{sprg} = 3.1585\beta + 80.9502\beta^2 + 580.4729\beta^3. \tag{4}$$

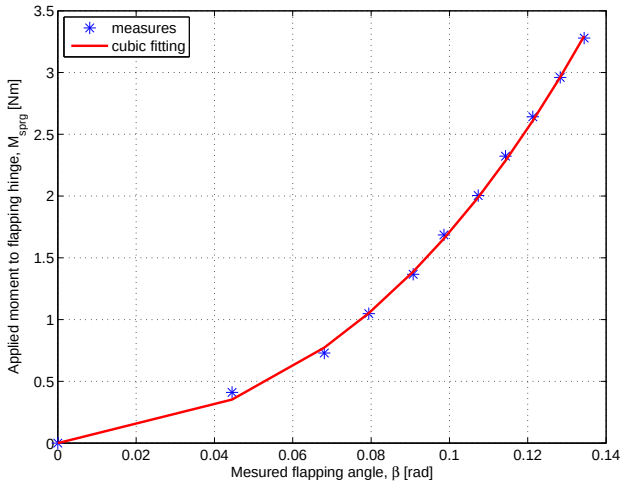

Figure 3: Experimental characterization results of rotor teetering articulation.

The equivalent flapping hinge offset can be calculated from the spring constant and blade centrifugal behavior. The moment about the blade flapping hinge is given by (see[7]):

$$M_{C.F.} = \Omega^2 \beta \left(I_b + eM_b\right), \tag{5}$$

where Ω is the rotor angular velocity, e is the effective hinge offset, I_b and M_b are respectively the moment of inertia and the static moment of the blade about the flapping hinge. For a torsional spring of stiffness k mounted at the teetering hub, the moment is (see[5]):

$$M_{sprg} = \Omega^2 \beta I_b + \beta k. \tag{6}$$

The two moments above defined are equal, hence the spring will behave the same as a hinge offset, defining an equivalent hinge offset:

$$e_{eqv} = \frac{k}{\Omega^2 M_b}. \tag{7}$$

For each test point in forward flight rotor attitude, defined by a value of incident velocity V_∞, rotor angle of attack respect to incident velocity α_s (measured from shaft plane direction, orthogonal to rotor shaft) and blade collective pitch angle θ_0, the implemented model algorithm imposes a initial guess value for the equivalent torsional spring stiffness k (hence for the equivalent hinge offset e_{eqv}) and it computes the first iteration of desired quantities.
First some basic parameters definition are recalled. The advance ratio:

$$\mu = \frac{V_\infty}{\Omega R} cos\alpha_s, \tag{8}$$

where R is the rotor radius.
The rotor induced velocity in hovering:

$$v_{i_{hov}} = \sqrt{\frac{T}{2\rho A}}, \tag{9}$$

where ρ is the air density, A the rotor disk area and T the rotor thrust value from hover tower test correspondent to considered collective pitch value.
The induced velocity in forward flight:

$$v_i = \sqrt{-\frac{{V_\infty}^2}{2} + \sqrt{\left(\frac{{V_\infty}^2}{2}\right)^2 + {v_{i_{hov}}}^4}}, \tag{10}$$

in the exact form, also valid for low speed.
Hence adopting the BET closed-form equations in[7], it is determined the thrust coefficient divided by solidity

$$C_T/\sigma = \left(1 - \frac{e_{eqv}}{R}\right)\frac{a}{4}\left[\theta_0\left(\frac{2}{3} + \mu^2\right) + \theta_1\left(\frac{1}{2} + \frac{\mu^2}{2}\right) + \mu\alpha_s - \frac{v_i}{\Omega R}\right], \tag{11}$$

where θ_1 is the linear built-in twist of blades and the longitudinal cyclic pitch B_1 is clearly imposed null for a quadrotor.

The first harmonic Fourier coefficients of the flapping motion about the offset flapping hinge considered (assuming the blades as rigid bodies) are: the coning a_0, the longitudinal flapping a_{1_s} and the lateral flapping b_{1_s}, defined below in the closed-form (adopting non-uniform inflow assumption).

$$a_0 = \frac{2}{3}\gamma\frac{C_T/\sigma}{a} - \frac{\frac{3}{2}gR^2}{(\Omega R)^2}, \tag{12}$$

where g is the gravity acceleration and γ is the Lock number

$$\gamma = \frac{c\rho a R^4}{I_b}, \tag{13}$$

where c is the blade chord.

(14)
$$a_{1_s} = \frac{\mu}{1-\frac{\mu^2}{2}}\left[\frac{16C_T/\sigma}{a} - 2\mu\alpha_s - 4\mu^2\left(\theta_0 + \frac{1}{2}\theta_1\right) + \frac{2v_i}{\Omega R}\right],$$

where again the longitudinal cyclic pitch B_1 is null.

(15)
$$b_{1_s} = \frac{\frac{4}{3}\mu a_0 + \frac{v_i}{\Omega R}}{1+\mu^2/2},$$

with the lateral cyclic pitch A_1 clearly imposed null for a quadrotor.
From the first iteration it is known the flapping angle, therefore it is possible to calculate the corresponding spring moment and the spring stiffness, obtaining the new value of equivalent hinge offset and iterate the calculation while the relative difference of spring stiffness between two iteration becomes smaller than a certain tolerance. The convergence is assured in few iterations.
Once obtained the thrust coefficient from previous iterative algorithm, it can be performed the calculation of rotor power for each test point in forward flight. From Equation 2 it is obtained the average blade angle of attack and then the drag coefficient is given by Equation 3. The incidence of rotor tip-path-plane (TPP) is defined as

(16)
$$\alpha_{TPP} = \alpha_s + a_{1_s},$$

and the inflow ratio is given by

(17)
$$\lambda = \frac{V_\infty sin\,\alpha_{TPP}}{\Omega R} - \frac{v_i}{\Omega R} = \mu\, tan\,\alpha_{TPP} - \lambda_i.$$

Finally the rotor torque coefficient divided by solidity in closed-form is obtained as

(18)
$$C_Q/\sigma = \frac{C_d}{8}\left(1+\mu^2\right) - \frac{a}{4}\left(\frac{\lambda}{1+\frac{3}{2}\mu^2}\right)\left[\frac{\theta_0}{3}\left(2-\mu^2\right) + \frac{\theta_1}{2}\left(1-\frac{\mu^2}{2}\right) + \lambda\left(1+\frac{\mu^2}{2}\right)\right] - \frac{a}{4}\left(\frac{\mu^2}{1+\frac{1}{2}\mu^2}\right)\left[\frac{{a_0}^2}{2}\left(\frac{1}{9}+\frac{\mu^2}{2}\right) + \frac{1}{3}\mu a_0\frac{v_i}{\Omega R} + \frac{1}{8}\left(\frac{v_i}{\Omega R}\right)^2\right],$$

from which the mechanical power is simply achieved converting the torque coefficient in dimensional form. The electrical power is obtained from the mechanical one through the motor-transmission global efficiency, taking into account mechanical and electrical losses, known from hover tower test as function of rotor power.
The last output desired from model is the rotor H-force in forward flight condition. The relative coefficient (divided by solidity) is given by the following closed-form formula

(19)
$$C_H/\sigma = \frac{C_d\mu}{4} - \frac{a}{4}\left(\frac{\mu\lambda}{1+\frac{3}{2}\mu^2}\right)\left[\theta_0\left(-\frac{1}{3}+\frac{3}{2}\mu^2\right) + \frac{\theta_1}{2}\left(-1+\frac{3}{2}\mu^2\right) - \lambda\right] + a_{1_s}C_T/\sigma + \frac{a}{4}\left(\frac{\mu}{1+\frac{1}{2}\mu^2}\right)\left[\frac{{a_0}^2}{2}\left(\frac{1}{9}+\frac{\mu^2}{2}\right) + \frac{1}{3}\mu a_0\frac{v_i}{\Omega R} + \frac{1}{8}\left(\frac{v_i}{\Omega R}\right)^2\right].$$

3. ANALYTICAL MODEL ADOPTED FOR DESCENT CONDITION

This section describes the adopted model to analyze the rotor behavior in descent: it is considered not only a perfect axial flow condition, with rotor plane orthogonal to the incident velocity directed upward respect to disk, but also different angles that implies an horizontal (forward) velocity component. The goal is to characterize the rotor mean inflow, varying independently the three parameters, incident velocity, rotor angle of attack respect to incident velocity and blade collective pitch angle, in particular in the critical Vortex Ring State (VRS) working condition.
A rotor operates in VRS when it is descending at low or null forward speed (steep descent) with a vertical velocity that approaches the value of the wake-induced velocity at the rotor disk. In this condition the rotor tip vortices are not convected away from disk rapidly enough, and the wake builds up and periodically breaks away. The tip vortices collect in a vortex ring, producing a circulating flow down through the rotor disk, then outward and upward outside the disk. The resulting flow is unsteady, hence a source of considerable low frequency vibration and possible control problems.

Some useful definitions from[8] are recalled below. The flow state of a rotor depends on the vertical velocity V_z (positive for climb) and horizontal velocity V_x (alternatively, using the rotor angle of attack α_s, $V_z = -V_x tan\,\alpha_s$). Hence in the context of momentum theory the mean induced velocity through the rotor disk is rigorously defined as:

(20)
$$\frac{v_i}{v_{i_{hov}}} = \frac{P_i}{P_{hov}} = f\left(\frac{V_z}{v_{i_{hov}}}, \frac{V_x}{v_{i_{hov}}}\right),$$

where $P_{hov} = Tv_{i_{hov}}$ is the ideal hover power and the appropriate velocity scale of the flow is the rotor induced velocity in hovering (given by Equation 9), adopted to obtain dimensionless velocity components.
The momentum theory solution in axial flow is given by

(21)
$$v_i = -\left(\frac{V_z}{2}\right) + \sqrt{\left(\frac{V_z}{2}\right)^2 + {v_{i_{hov}}}^2}$$

for $V_z > 0$, and

$$v_i = -\left(\frac{V_z}{2}\right) \pm \sqrt{\left(\frac{V_z}{2}\right)^2 - {v_{i_{hov}}}^2} \tag{22}$$

for $V_z < -2v_{i_{hov}}$, as shown in Figure 4. The total velocities in the far field, at the rotor disk, and in the far wake are V_z, $V_z + v_i$, and $V_z + 2v_i$ respectively, and the plotted lines $V_z = 0$, $V_z + v_i = 0$, and $V_z + 2v_i = 0$ define the limits of different axial flow states regions as indicated in Figure 4. Only for climb ($V_z > 0$) and windmill brake state is the velocity in the same direction throughout the flow field, so the momentum theory is strictly valid. For small rates of descent, the flow near the rotor disk is similar to that assumed by momentum theory, and it is found that the momentum theory solution still gives a reasonable estimate of the power. But as the descent rate increases (vortex ring and turbulent wake state), the total velocity through the disk $V_z + v_i$ approaches zero, implying that the wake is not being convected away from the disk and the momentum theory is no longer valid.
The momentum theory expression for the induced velocity in forward flight as well as axial flow is given by the Glauert formula[8]:

$$v_i = \frac{{v_{i_{hov}}}^2}{\sqrt{{V_x}^2 + (V_z + v_i)^2}}. \tag{23}$$

Figure 5 shows the solution for different values of horizontal velocity V_x. In forward flight ($V_x > 0$) the singularity of momentum theory at ideal autorotation ($V_z + v_i = 0$) is eliminated, but it is expected that the result is still invalid near $V_z + v_i = 0$ until V_x is sufficiently large, that is, until V_x produces sufficient mass flow through the rotor disk and convects the wake away from the disk.

In order to have a reliable model for the rotor inflow in the working states when the momentum theory is invalid, with computation complexity suitable for flight dynamics purposes, the solution developed in[8] was implemented: it consists in a parametric extension of momentum theory for calculation of mean induced velocity in VRS based on existing in literature flight test and wind tunnel test data on both helicopters and tilt-rotors.
Measurements of the global performance (power and thrust) of a rotor can be used to calculate the mean induced velocity (called P&T method in[8]) and in particular test data must be the basis to find rotor inflow in vortex ring state and turbulent wake state. From the definition of the induced velocity it follows that

$$V_z + v_i = \frac{P - P_0}{T}, \tag{24}$$

where P is the total rotor power and P_0 is the profile power. This result depends on the estimate of profile power from model considered constant, independent of the climb/descent rate and forward speed (reasonable assumption at least for low advance ratio, as in this work).
The VRS model proposed in[8] first establishes a vortex ring state stability boundary as a function of dimensionless V_x and V_z, based on the helicopters and tilt-rotors available test data; this stability boundary is where the inflow curve has zero slope, $d(V_z + v_i)/dV_z = 0$, and it is defined such that it encloses most of the available test point in literature.
Then the inflow curve in VRS is defined through two steps. The first is to eliminate the singularity of momentum theory at ideal autorotation in vertical descent. The result of this step is referred to as the baseline model. The second step is to create the region of negative slope in vortex ring state. For both steps, third order polynomials are identified: they provide the required behavior of the inflow as a function of scaled V_z and V_x, joining the momentum theory curves in the validity regions, and the final result is reported in Figure 6.
Comparing Figure 6 with Figure 5 it is clear that the Glauert formulation for the inflow is considered valid for dimensionless horizontal velocity values greater than 1 (for any dimensionless vertical velocity component), while below this value the VRS model correction is necessary: in particular the VRS stability boundary limit on dimensionless horizontal velocity is 0.95 (see Figure 19).
For further details about the VRS model algorithm refer to[8].

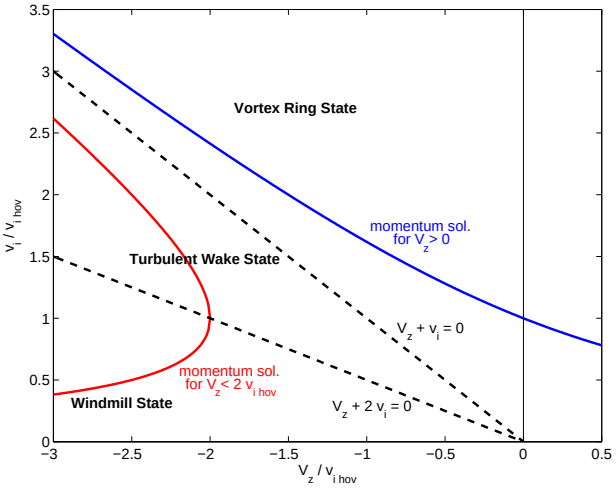

Figure 4: Rotor inflow states in axial flow. Normal working state when $V_z > 0$; vortex ring state when $V_z < 0$, $V_z + v_i > 0$; turbulent wake state when $V_z < 0$, $V_z + v_i < 0$, $V_z + 2v_i > 0$; windmill brake state when $V_z < 0$, $V_z + 2v_i < 0$.

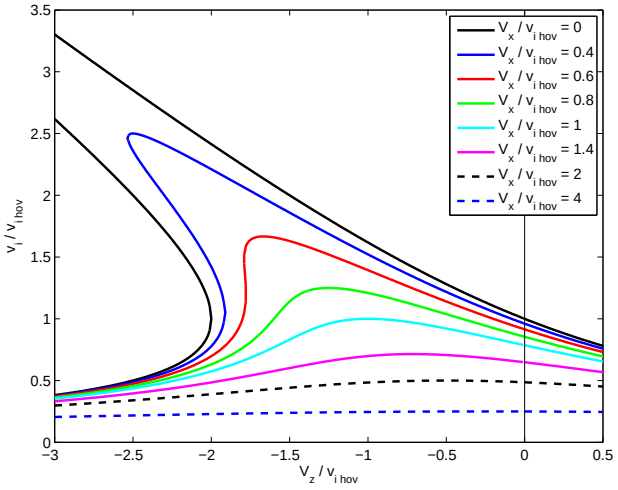

Figure 5: Rotor inflow from Glauert formulation.

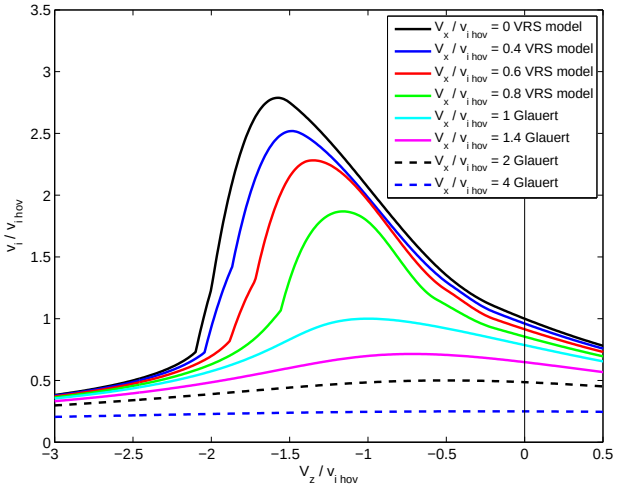

Figure 6: Rotor inflow from VRS model.

4. WIND TUNNEL TESTING

In this section will be provided some details about the experimental activities conducted on the considered full-scale isolated rotor at Politecnico di Milano wind tunnel (GVPM), in the aeronautical test section ($w = 4$ m width, $h = 3.84$ m height), with the aim of minimizing duration and equipment costs.
The selection of test points matrix, varying wind velocity, rotor angle of attack respect to incident velocity and collective pitch, was made considering the following guidelines and constraints:

- single day test duration;
- avoid test points at velocity lower than 2 m/s (wind tunnel flow instability expected under this limits);
- avoid test points with expected electrical power (from analytical model) greater than 350 W (maximum continuous motor limit);
- avoid test points with expected electrical power lower than 0 W (windmill state): not manageable electrical working condition;
- cover the ANTEOS A2-MINI/B flight envelope (maximum velocity is about 10 m/s);

Finally the wind tunnel test points matrix for each rotor angle of attack is represented in Table 2, to be performed for the following rotor AoA: -30°, -20°, -10°, -5°, 5°, 10°, 20°, 45°, 75°, 90° (negative value indicates forward flight regime, 90° is the axial descent).

Collective pitch		Wind tunnel velocity [m/s]				
[%]	[deg]	2	4	6	8	10
20	4.2	-	-	-	-	-
40	7.2	-	-	-	-	-
60	9.6	-	-	-	-	-
80	12.1	-	-	-	-	-
90	13.5	-	-	-	-	-

Table 2: Wind tunnel test points matrix for each rotor AoA. Collective pitch reported in both command percentage and angle.

Cause campaign duration constraint the following test point of above scheduled matrix was skipped:

- velocity 6, 8, 10 m/s at rotor AoA 75° and 90°
- velocity 8, 10 m/s at rotor AoA 45°

4.1 Rotor test-bed details

A suitable test-bed was designed and realized in order to accommodate the full scale complete motor-rotor system. A pylon, made-up by two beam of circular section in aluminum alloy connected together, brings the rotor center in the middle of test section (1.92 m from wind tunnel floor). To the upper part of the pylon is connected the rotor AoA changing device, on which is mounted the structure interfacing the motor/rotor group with the load cell. The angle is varied manually (checked by a digital inclinometer) in the simplest and cheapest way, rotating the motor/rotor/load cell group.
A FEM model of the test-bed structure was developed, performing static analysis under expected worst case load and eigenvalue analysis, in order to assure reduced deformations and avoid resonance with the rotor harmonics.
Figure 7 shows the complete experimental set-up in the wind tunnel section and Figure 8 depicts some details.
During the experiments the following quantities were acquired and logged:

- forces and moments in rotor shaft reference frame using a 6 axis load cell (sampling frequency 2 KHz): suitable full scale was selected exploiting analytical model estimates;
- wind tunnel test section air data: density, temperature, velocity;
- motor parameters (electric power, voltage, temperature) and rotor RPM (Hall effect sensor on rotor shaft), sampled at 50 Hz ;

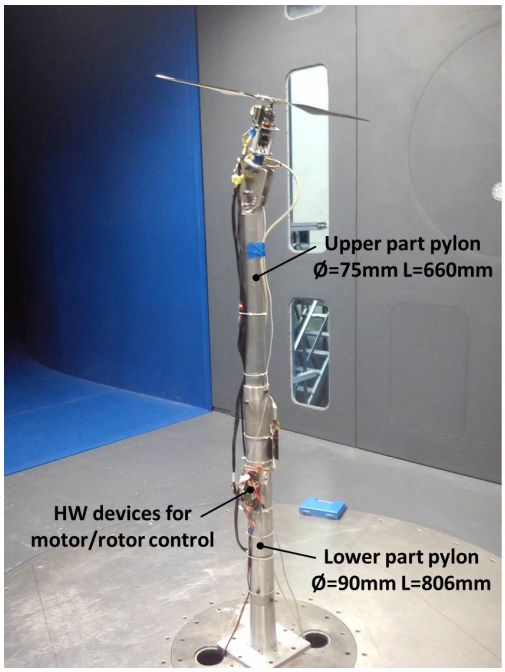

Figure 7: Wind tunnel experimental set-up.

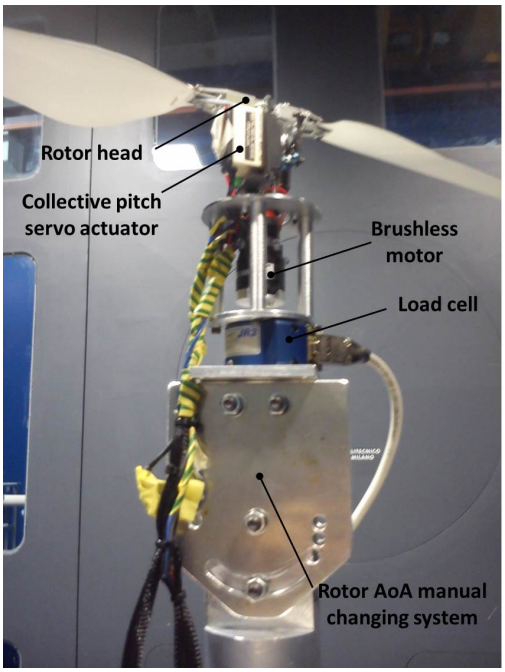

Figure 8: Test-bed and rotor system details.

- commanded collective pitch;
- measures from tri-axial accelerometer (sampling frequency 2 KHz), in order to monitoring changes in vibration spectrum varying rotor working conditions (expected vibration increase in VRS);
- high frame rate camera, with strobe light and shutter synchronized with rotor RPM measure, in side view positioning respect to rotor with background reference grid, in order to measure from images the rotor plane attitude.

A proper software interface was available in order to control from a computer (through a LAN connection) the rotor power on/off and the collective pitch, and monitor in real-time some critical parameters: rotor RPM, motor data, vibration spectrum. Considering the adopted non-automated system for varying the rotor AoA, for its every change the wind tunnel was stopped in order to accede the test section: the operation takes about 5 minutes. The operating condition of each test point was maintained for about 1 minutes, on which compute the mean of logged parameters.

4.2 Aerodynamic interferences evaluation

Clearly aerodynamic interference due to the wind tunnel walls must be minimized and in any case taken into account in order to obtain data representative of the free-air operations. First of all it is guaranteed that the rotor operates out of ground effect with a distance from floor equal to about 5 times the rotor radius, when a minimum height of at least $2R$ is required to ensure performance measurements free from interference effects[9].

It is well known that the net effect of a wind tunnel closed test section is to produce an additional upwash at the rotor disk: the measured torque will be lower than the free-air value since rotor blades will experience (in average) an higher angle of attack for the same collective pitch. It is possible to reproduce this influence of the wind tunnel environment as a variation of the rotor shaft angle of attack and apply a proper shaft angle correction $\Delta\alpha_s$ to the analytical model input respect to the tested value α_s. The classical Glauert correction methodology was adopted (see[10]) by means of the following formula:

$$\Delta\alpha_s = \frac{180}{\pi}\frac{2\delta_{wt}C_T A}{\mu^2 A_{wt}}, \tag{25}$$

where A_{wt} is the test section area and δ_{wt} is the boundary correction factor (0.132) reported in[11] as function of the ratio between rotor diameter and test section width ($D/w = 0.1875$), given the test section aspect ratio ($h/w = 0.96$). The necessary shaft angle correction is limited thanks to the small rotor diameter respect to the test section dimensions (disk area is 2.9% of A_{wt}): lower than 1° for all the test points at 6, 8, 10 m/s in forward flight condition, up to a maximum of about 7° in the worst case of smallest advance ratio (about 0.02 at 2 m/s) and highest thrust coefficient.

Furthermore, at low speed and high rotor thrust conditions, a closed test section may experience what is known as *flow breakdown*, where the interaction between the rotor wake and the tunnel walls strongly modify the flow in the vicinity of the rotor due to the onset of recirculation (see[12],[10]): in this condition, the wind tunnel environment is no longer representative of the free-air operation and the rotor performance cannot be adjusted by means of wall corrections. In[12] is provided an early

attempt to identify flow breakdown boundary curves in terms of thrust coefficient and advance ratio for several rotor dimensions in square section tunnel: the smallest reported D/w is 0.2 (slightly above the considered case, worsen condition) and for the maximum tested C_T of about 0.01 flow breakdown is expected for advance ratio lower than approximately 0.04 (3 m/s). Hence the phenomena could occur only for test points executed at 2 m/s with collective pitch command greater than 60%. But the characterization in[12] is referred to the case of null rotor AoA and the increasing of the incidence (for testing forward flight regime) implies higher rotor wake skew angle, moving downstream the point where wake impinges on the floor, hence a shift of the breakdown occurrence limit to lower advance ratio should be expected. The phenomena is complex and is actually an open question as confirmed by the recent work[13], characterizing the Politecnico di Milano wind tunnel test section in a worse case of rotor with more than double diameter: it was validated the flow breakdown boundary limit predicted in[12].

Regarding the test-bed interferences, clearly they can not be completely removed: they are difficult to estimate accurately and depends basically on amount and position of test-bed surfaces respect to rotor disk and its wake. In particular, when the rotor AoA is null, all components of the test-bed under the rotor disk are into the root cut-out diameter and it is the minimum interference configuration. While when the AoA is 90° (vertical descent), the maximum test-bed cross section under the rotor is about 7.5% of disk area and the interferences are at the higher level. Furthermore in all descent configurations the rotor is behind the test-bed respect to the incident wind, hence the wind velocity is not uniform because it is perturbed by the support.
To take into account the above mentioned effects in the simplest way, obtaining a consistent comparison between experimental and analytical results, it was conducted a fixed point thrust test for each rotor AoA test-bed configuration: the rotor induced velocity in hovering from momentum theory (see Equation 9), used in the analytical model (both for forward and descent conditions) was calculated using the thrust value obtained from the fixed point test, for the corresponding AoA and collective pitch value. The Figure 9 shows the results of fixed point thrust test (varying the collective pitch) at AoA equal to 0° and 90° (minimum and maximum interference configurations) and the percentage delta (calculated respect to case AoA=0°) between the two cases in terms of rotor thrust and mechanical power.
In order to check the induced velocity evaluation using the P&T method and then evaluate the reliability of power and thrust measures during the test, in[8] is proposed the following approach. In practical applications of momentum theory, a multiplicative factor κ is introduced, $v_i = \kappa v_{i_{ideal}}$, to correct the ideal induced velocity for non-ideal induced losses: in hover κ varies from 1 to 1.15 typically.
The value of κ was evaluated for each test point of all hovering thrust test conducted at different AoA configurations: a reasonable value of factor κ, considering the above range, indicates that power and thrust measures are sufficiently reliable.
In upper Figure 10 is compared, as function of thrust coefficient scaled by solidity (then as function of collective pitch), the ideal induced velocity value, calculated with Equation 9 using the measured thrust value, and the actual induced velocity through Equation 24 of the P&T methods. The comparison is reported for fixed point thrust test at AoA=0° and 90° in order to evaluate also the test-bed interference on the measures. The consequent factor κ obtained is reported in lower Figure 10: values into the expected range confirms that power and thrust measures are reliable, also varying the rotor AoA.

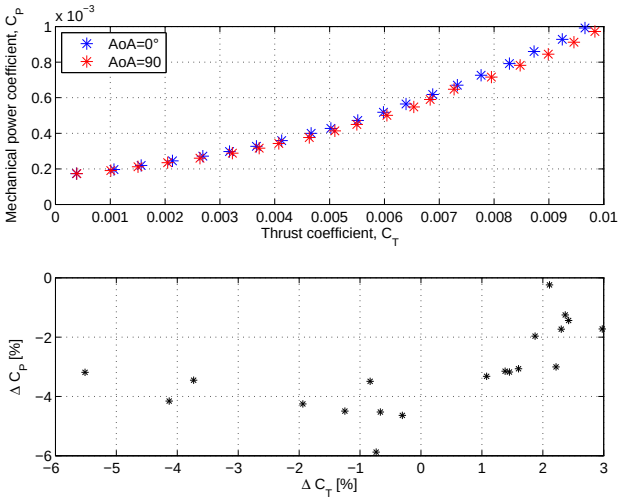

Figure 9: Fixed point thrust test results with test-bed configured with AoA=0° and 90° and percentage delta between the two cases.

4.3 Flapping angles measures

Longitudinal and lateral flapping angles measures are not straightforward to achieve. They can be obtained from blades root flapping angle measured using Rotary Variable Differential Transformers (RVDTs) mounted on blades flapping hinge or adopting laser distance transducers (and relative reflective objects) properly placed on the rotor head (see *e.g.*,[14] and the references therein). In both cases the rotor hub must be modified to accommodate the sensors and equipped with a slip ring assembly: complex and not viable solutions considering the small dimensions of the full scale rotor system under test.
An alternative method is the blades displacement measurements using multi-camera photogrammetry

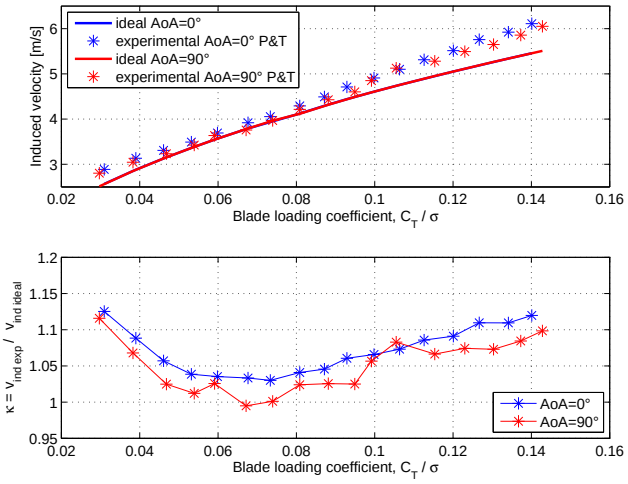

Figure 10: Upper: comparison ideal induced velocity *vs.* actual one obtained using P&T method on fixed point thrust test results, with test-bed configured with AoA=0° and 90°. Lower: corresponding induced velocity correction factor κ.

(see [15]), where the only modification to rotor system needed is the application of retro-reflective adhesive tape targets on blades surface. Clearly high-quality flapping angle data can be obtained, taking into account also the blades deformations (on the contrary of the previous methods), but adopting a very expensive system which requires tricky calibration activities, justifiable for CFD/CSD techniques validation.

The adopted simplest (and cheapest) strategy is to obtain flapping angles indirectly through the load cell forces measures, through the following steps (refer to Figures 11 and 12 for reference frames definition and forces nomenclature used):

1. measure force components in load cell reference frame, corresponding to rotor shaft reference frame: clearly set to zero of load cell was made before measuring (with rotor off) in order to subtract rotor/motor weight contribution and read only the aerodynamic resultant R_{aero} force components on shaft reference frame;
2. compute the R_{aero} module

$$(R_{aero})_{aero-ref} = (0, 0, |R_{aero}|)\,, \tag{26}$$

$$(R_{aero})_{shaft} = (F_x, F_y, F_z)\,. \tag{27}$$

3. compute the rotation vector (axis and angle representation) from $(R_{aero})_{aero-ref}$ to $(R_{aero})_{shaft}$;
4. pass to rotation matrix representation and extract angle $(a_{1_s} + \delta)$ and lateral flapping angle b_{1_s};
5. obtain the longitudinal flapping angle a_{1_s} using the estimate of δ angle from thrust T and H-force H values calculated by analytical model;
6. calculate rotation matrix (using a_{1_s} and b_{1_s}) from $(R_{aero})_{shaft}$ to $(R_{aero})_{TPP}$, where TPP indicates the rotor tip-path-plane;
7. find experimental values of rotor thrust and H-force considering that

$$(R_{aero})_{TPP} = (H, 0, T)\,. \tag{28}$$

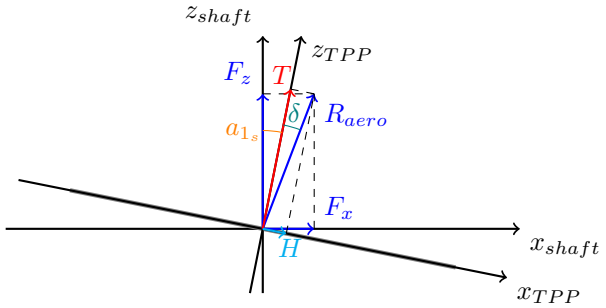

Figure 11: Rotor side view: reference frames and forces definition.

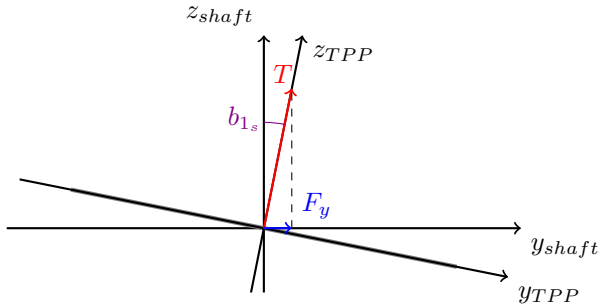

Figure 12: Rotor rear view: reference frames and forces definition.

Obviously the images taken with the high frame rate camera can be used to measure flapping angles. The side view positioning of camera respect to rotor is the simplest choice operating in the wind tunnel, and it can be useful to solve previous discussed ambiguities on longitudinal flapping angle extraction from load cell measures, which implies the use of analytical model. On the contrary the rear view camera positioning was not considered because lateral flapping can be directly obtained from load cell measures as explained above.
The initial intent of using the images in order to determine longitudinal flapping angle turned out to be not feasible once executed the test: the expected longitudinal flapping angles from analytical model are small (not above 5°), and the angular resolution in evaluate it from images (using the reference grid) is not enough to detect it properly: rotor plane vibrations influence negatively the images sharpness and it is difficult to discern flapping from coning.
Therefore the camera images were not used and both flapping angles were determined from load cell measures adopting the procedure illustrated above.

5. COMPARISON BETWEEN EXPERIMENTAL AND ANALYTICAL MODEL RESULTS

5.1 Forward flight conditions

This section presents the results about the rotor global performance parameters (thrust, power, H-force) in forward flight conditions in terms of rotor AoA. For sake of conciseness only a representative selection of whole data processing is showed from Figure 13 to 16: in general a good correlation between analytical model estimates and the wind tunnel experimental values can be appreciated, confirming that the simplifying assumption adopted for the closed-form BET based model are suitable for flight mechanics purposes. Moreover it emerges that adopted shaft angle correction for wind tunnel walls effects was adequate.

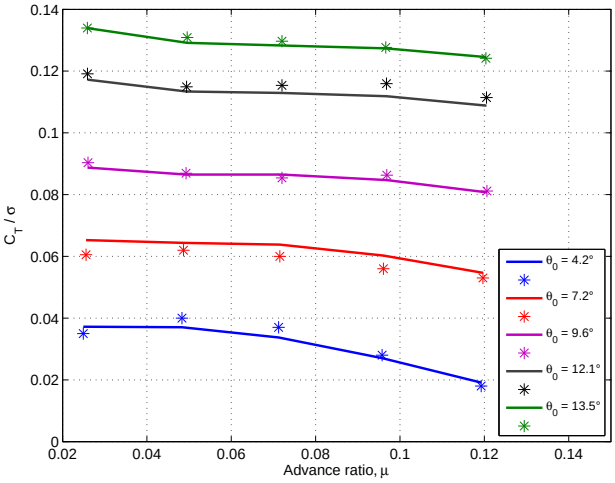

Figure 13: Analytical thrust coefficient divided by solidity (lines) *vs.* experimental test point (∗) as function of μ, rotor AoA = -20°, varying the collective pitch.

It is worth to observe in Figure 15 a slight increase of mismatch of rotor power measures respect to model for the two test points at high collective pitch (80% and 90% command) and lowest advance ratio (about 0.025, correspondent to 2 m/s velocity), with rotor AoA at -5°. As discussed in Section 4.2, considering the flow breakdown limit evaluation, the condition could be expected only for test points executed at 2 m/s with collective pitch command greater than 60%, but considering the rotor with null AoA (horizontal). The lower measured power in the two test points respect to model, representing the free-air value, indicates a slightly insufficient shaft angle correction probably due to an incipient flow breakdown.

Regarding the flapping angles, the experimental values obtained indirectly from load cell logged forces (passing through the model) are not always reliable.

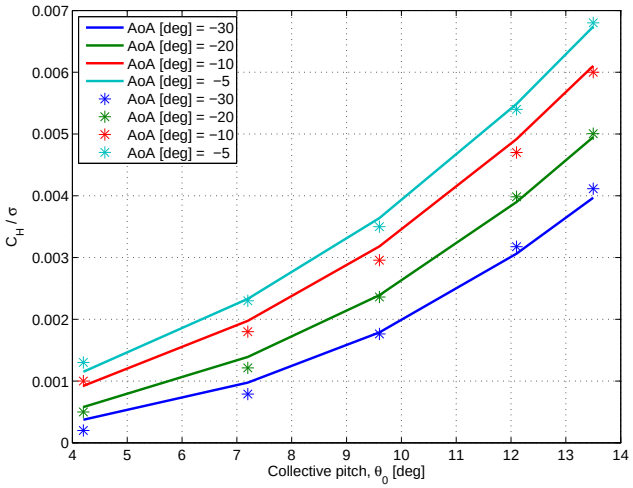

Figure 14: Analytical H-force coefficient divided by solidity (lines) *vs.* experimental test point (∗) as function of collective pitch, velocity = 6 m/s, varying the rotor AoA.

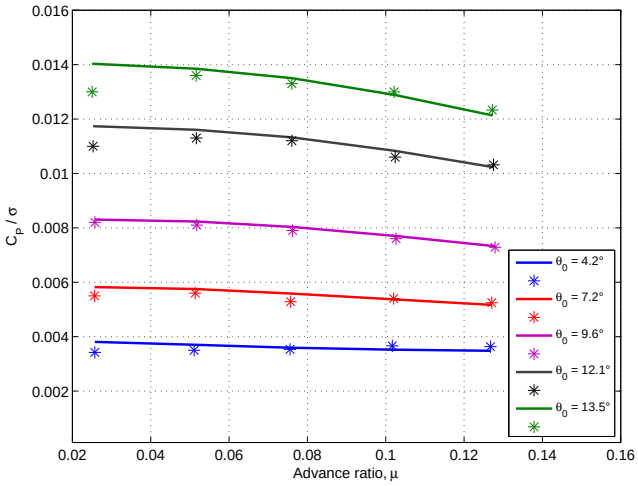

Figure 15: Analytical mechanical power coefficient divided by solidity (lines) *vs.* experimental test point (∗) as function of μ, rotor AoA = -5°, varying the collective pitch.

The main reason is that lateral rotor force component measured from load cell is noisy and at the same time the magnitude to be detected is small (as confirmed by model estimate), then this corrupted data heavily affect the flapping angles calculation in some cases. Moreover also the analytical model used for flapping angles evaluation presents some limits, mostly for the very low advance ratio experienced in this study.
Figure 17 shows the comparison between experimental and analytical values of longitudinal flapping angle as function of advance ratio, varying the rotor AoA, for different collective pitch command set (outlier test points were omitted). The observed behavior is qualitatively in agreement with expected from previous rotor characterization at low advance ratio: as reported in[7] and[16] the closed-form BET approach fairly underestimate the experimental longitudinal

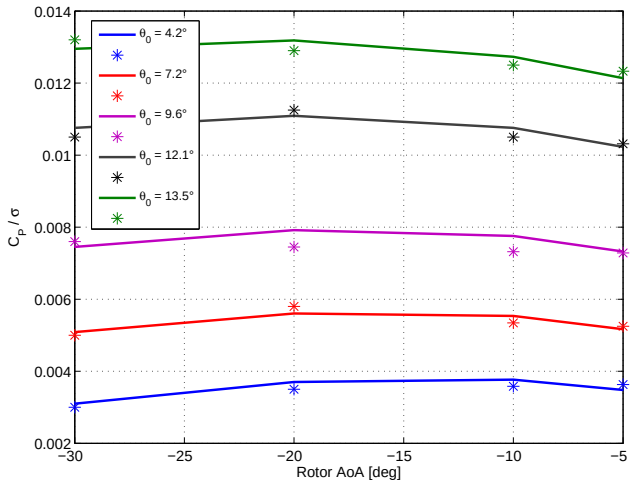

Figure 16: Analytical mechanical power coefficient divided by solidity (lines) *vs.* experimental test point ($*$) as function of rotor AoA, velocity = 10 m/s, varying the collective pitch.

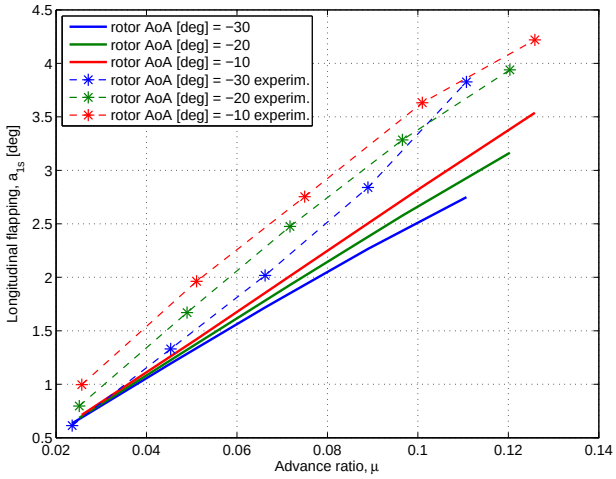

(a) Collective pitch 80% (θ_0=12.1°)

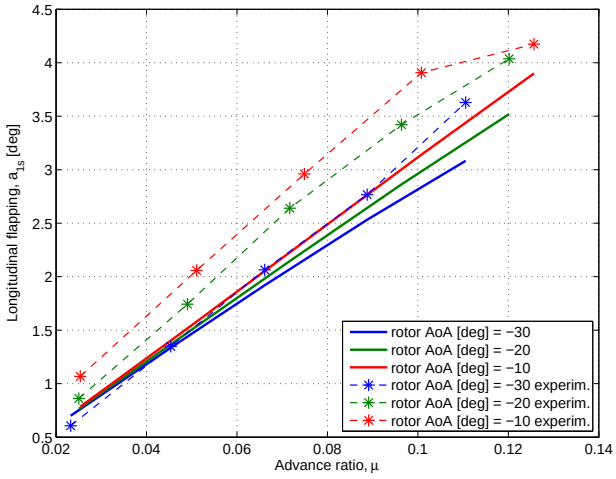

(b) Collective pitch 90% (θ_0=13.5°)

Figure 17: Analytical rotor longitudinal flapping angle (lines) *vs.* experimental test point ($*$) as function of advance ratio, varying rotor AoA, for different collective pitch command.

flapping angle.

Figure 18 shows the results for the lateral flapping angle (again outlier test points were omitted). Two different analytical results were reported: adopting the Equation 15 for non-uniform inflow and the following closed-form equation for uniform inflow assumption:

$$b_{1_s} = \frac{\frac{4}{3}\mu a_0}{1+\mu^2/2}. \tag{29}$$

The observed behavior is qualitatively in agreement with results reported in[16] and[17]: lateral flapping is highly sensitive to non-uniform inflow distribution over the rotor disk, then it can not be rigorously calculated without determination of the wake-induced inflow velocities especially at low advance ratios, when is necessary the use of free wake geometry calculation.

5.2 Descent conditions

In this section the results obtained from implemented analytical model for descent working conditions (see Section 3) will be presented and compared with the results from wind tunnel experimental campaign.
The executed wind tunnel test points in descent are reported in Figure 19, as function of horizontal and vertical non-dimensional component of incident velocity (then function of wind velocity and rotor AoA), pointing out which are in and out the VRS stability boundary defined by the model.
Figure 20 shows the rotor induced velocity as function of horizontal and vertical component of incident velocity (all scaled quantities by induced velocity in hovering) from the analytical model. The experimental mean inflow values, obtained from power and thrust measures through the knowledge of profile power from model (P&T method, see 3), are superimposed: it is worth to observe only few outlier test points respect to model estimation trend.

In order to evaluate with more detail the level of matching between the experimental data and the analytical model, bidimensional representations of the previous surface plot of Figure 20 are reported in Figures 21 and 22. For sake of conciseness only a selection of test points is shown, choosing the test conditions in terms of wind velocity and collective pitch in which almost one test point into VRS boundary was present. The obtained results show a good correlation analytic *vs.* experimental for the rotor mean inflow, in particular for test point into VRS boundary, therefore the empirical extension of momentum theory proposed in[8] is suitable for this type of rotor.

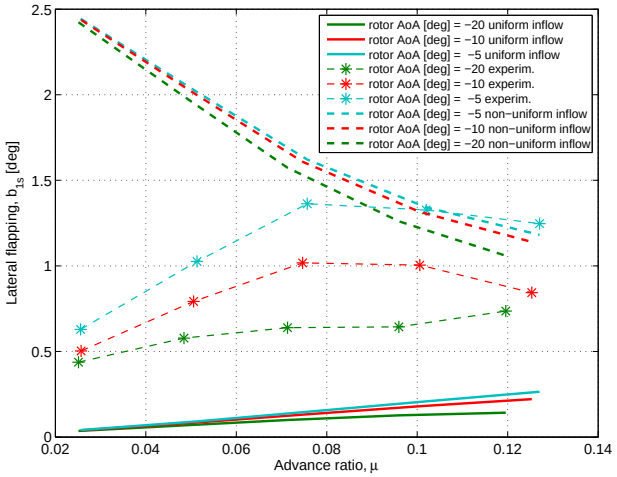

(a) Collective pitch 40% (θ_0=7.2°)

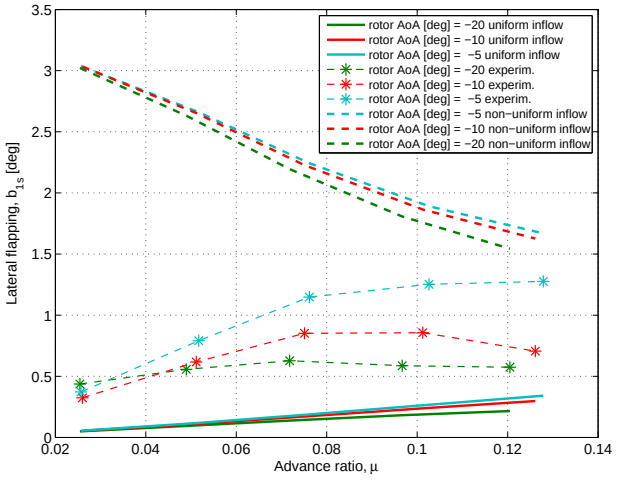

(b) Collective pitch 60% (θ_0=9.6°)

Figure 18: Analytical rotor lateral flapping angle (lines) *vs.* experimental test point ($*$) as function of advance ratio, varying rotor AoA, for different collective pitch command.

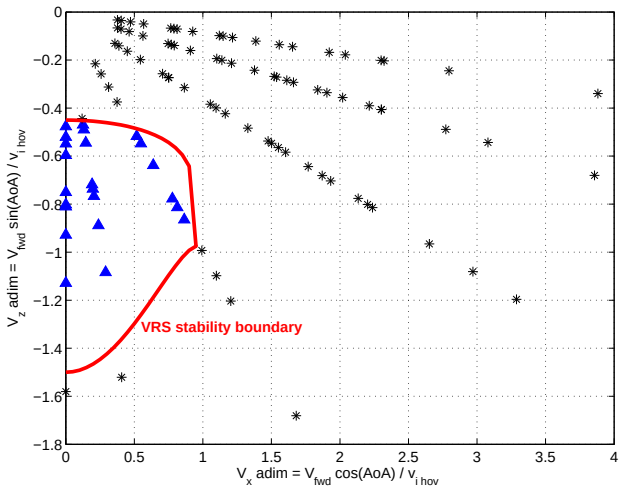

Figure 19: Executed test point in descent in terms of horizontal and vertical non-dimensional incident velocity. VRS stability boundary defined by the model is showed: test point into VRS depicted with ▲, out with $*$.

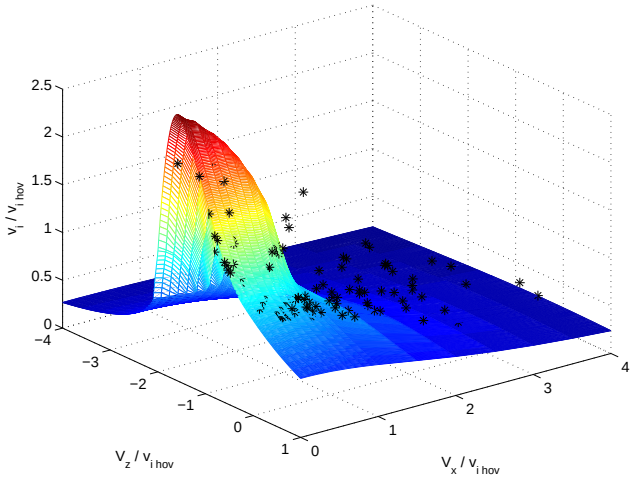

Figure 20: Analytical rotor mean induced velocity *vs.* experimental test point ($*$) as function of horizontal and vertical incident velocity on rotor. All velocities are scaled by induced velocity in hovering.

6. CONTROL SYNTHESIS APPLICATIONS USING THE DEVELOPED MODEL

The experimentally validated model for rotor aerodynamics was coupled with quadrotor rigid body equations of motion and adopted for peculiar control synthesis applications, specifically addressed to variable-pitch architecture, in cases where an adequate rotor modeling detail is needed to capture correctly the vehicle dynamics and accordingly design the control law.

A control strategy to safely recover a one rotor complete loss of thrust performing an emergency landing was proposed in[18]. Clearly the control of yaw DoF is no more possible and vehicle enters a spin mode with high steady state angular velocity. Exploiting the variable-pitch architecture, it is possible to avoid the vehicle "flip" around roll or pitch axis in the instant of thrust loss (inevitable with a fixed pitch configuration) generating a negative thrust on the rotor opposite to the faulty one. When spin in yaw is developed it becomes possible to control the roll and pitch DoFs by actuating periodically rotors thrust corrections as functions of azimuthal position of rotors during revolution in yaw, performing a steep descent (encountering VRS regime).

Another application of developed model can be found in[19]. The problem of maximizing the rotors figure of merit by scheduling the fixed rotors RPM set (for a variable-pitch quadrotor) as function of trimmed forward flight velocity was considered, demonstrating that power savings (and hence endurance increments) can be achieved (critical aspect for electrically powered UAVs). Subsequently the design of longitudinal dynamics controller was carried out, showing that a simple gain-scheduling strategy can be

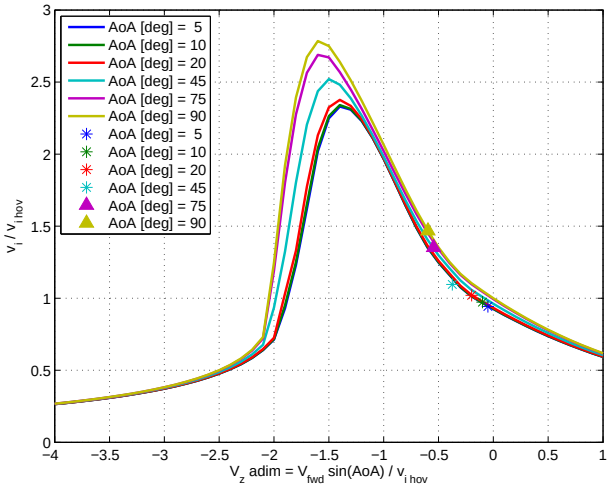

(a) Collective pitch 40% (θ_0=7.2°)

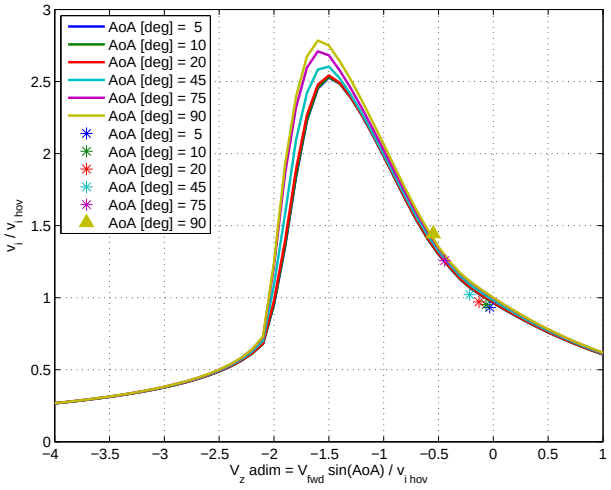

(b) Collective pitch 90% (θ_0=13.5°)

Figure 21: Analytical dimensionless induced velocity (lines) *vs.* experimental data as function of dimensionless vertical incident velocity, wind tunnel velocity of 2 m/s, varying rotor AoA, for different collective pitch command. Test point into VRS depicted with ▲, out with ∗.

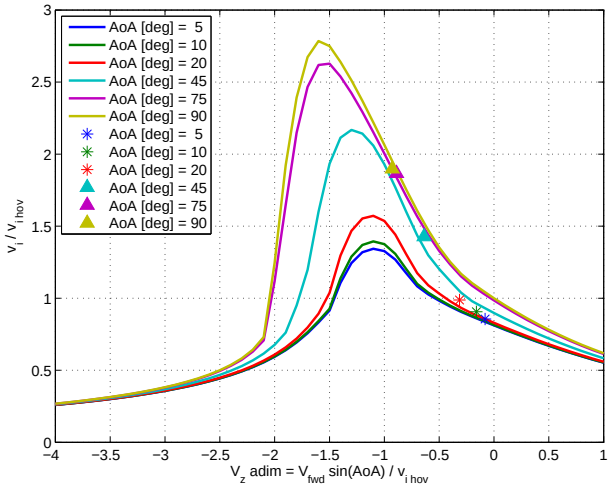

(a) Collective pitch 60% (θ_0=9.6°)

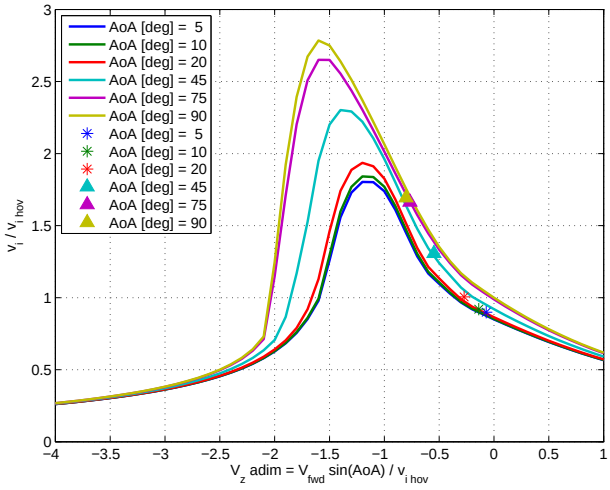

(b) Collective pitch 80% (θ_0=12.1°)

Figure 22: Analytical dimensionless induced velocity (lines) *vs.* experimental data as function of dimensionless vertical incident velocity, wind tunnel velocity of 4 m/s, varying rotor AoA, for different collective pitch command. Test point into VRS depicted with ▲, out with ∗.

adopted to recover uniform handling qualities for trim conditions corresponding to different values of vehicle speed (and accordingly rotors angular velocity).

7. CONCLUDING REMARKS

In this paper the aerodynamics characterization of a commercial quadrotor UAV isolated rotor through a wind tunnel testing campaign (minimizing duration and equipments costs) on the full scale rotor system was discussed, which is distinguished respect to most common small quadrotor by the variable-pitch configuration and the teetering articulation. The aim was to evaluate the rotor global performance (thrust, power, H-force) and the flapping angle in forward flight and the mean induced inflow in descent, in particular in VRS condition. The wind tunnel test points matrix was selected in order to cover the vehicle flight envelope, considering non trimmed conditions in terms of velocity, rotor attitude and collective pitch.

The aerodynamic interference effects due to wind tunnel walls (including flow breakdown) and test-bed was evaluated, applying the proper correction in processing the data.

A suitable rotor aerodynamics analytical model for flight mechanics purposes was developed, based on BET closed-form equations, adopting an empirical parametric extension of momentum theory for calculation of mean induced velocity in VRS. The good results in terms of matching between analytical estimate and experimental data confirm the validity of the adopted model, concerning the rotor global performance and mean inflow in both forward flight and descent conditions. Regarding the flapping angle, the model is fairly adequate for the longitudinal component while for the lateral one a more refined model is

required to calculate precisely the non-uniform inflow distribution over the rotor disk.
Finally some specific quadrotor control synthesis applications, using the validated rotor aerodynamics model, were briefly presented (citing the dedicated works).

ACKNOWLEDGMENTS

The author wish to thank: Prof. Carlo Luigi Bottasso (Politecnico di Milano) for the work supervision, Aermatica SpA which provided the rotor system, Mr. Gabriele Campanardi and Mr. Donato Grassi (Politecnico di Milano wind tunnel technicians) and Mr. Andrea Zanin (Aermatica R&D laboratory) for their collaboration.

REFERENCES

[1] Mahony, R., Kumar, V. and Corke, P. Multirotor Aerial Vehicles: Modeling, Estimation and Control of Quadrotor. *IEEE Robotics & Automation Magazine*, 19(3):20–32, 2012.

[2] Hoffmann, G.M., Huang, H., Waslander, S.L. and Tomlin, C.J. Quadrotor Helicopter Flight Dynamics and Control: Theory and Experiment. In *AIAA Guidance, Navigation, and Control Conference, Hilton Head, SC, USA*, 2007.

[3] Huang, H., Hoffmann, G.M., Waslander, S.L. and Tomlin, C.J. Aerodynamics and Control of Autonomous Quadrotor Helicopters in Aggressive Maneuvering. In *IEEE International Conference on Robotics and Automation (ICRA), Kobe, Japan*, pages 3277–3282, 2009.

[4] Bristeau, P., Martin, P., Salaün, E. and Petit, N. The Role of Propeller Aerodynamics in the Model of a Quadrotor UAV. In *European Control Conference, Budapest, Hungary*, pages 683–688, 2009.

[5] Pounds, P., Mahony, R. and Gresham, J. Towards Dynamically-Favourable Quad-Rotor Aerial Robots. In *Australasian Conference on Robotics and Automation, Canberra, Australia*, 2004.

[6] Kaya, D. and Kutay, A. T. Aerodynamic Modeling and Parameter Estimation of a Quadrotor Helicopter. In *AIAA Atmospheric Flight Mechanics Conference , Atlanta, GA, USA*, 2014.

[7] Prouty, R.W. *Helicopter Performance, Stability, and Control.* Krieger Publishing Company, 1986.

[8] Johnson, W. Model for Vortex Ring State Influence on Rotorcraft Flight Dynamics. *NASA TP-2005-213477*, 2005.

[9] Leishman, J. G. *Principles of Helicopter Aerodynamics, 2nd ed.* Cambridge University Press, New York, NY, 2006.

[10] Langer, H.-J., Peterson, R. L. and Maier, T. H. An Experimental Evaluation of Wind Tunnel Wall Correction Methods for Helicopter Performance. In *52th Annual Forum of the American Helicopter Society, Washington, DC*, 1996.

[11] Barlow, J. B., Rae, W. H. and Pope, A. *Low-Speed Wind Tunnel Testing, 3rd ed.* John Wiley & Sons, Inc., 1999.

[12] Harris, F. D. Aerodynamic and Dynamic Rotary Wing Model Testing in Wind Tunnels and Other Facilities. In *AGARD LS 63, Helicopter Aerodynamics and Dynamics*, 1973.

[13] Biava, M. and Vigevano, L. Computational Assessment of Wind Tunnel Flow in Closed and Open Section Model Rotor Tests. *Journal of the American Helicopter Society*, 59(1):1–17, 2014.

[14] Fletcher, J. W. and Tischler, M. B. Improving Helicopter Flight Mechanics Models with Laser Measurement of Blade Flapping. In *53th Annual Forum of the American Helicopter Society*, Virginia Beach, VA, April 29 - May 1 1997.

[15] Abrego, A. I., Olson, L. E., Romander, E. A., Barrows, D. A. and Burner, A. W. Blade Displacement Measurement Technique Applied to a Full-Scale Rotor Test. In *68th Annual Forum of the American Helicopter Society*, Fort Worth, Texas, May 1 - 3 2012.

[16] Harris, F. D. Articulated Rotor Blade Flapping Motion at Low Advance Ratio. *Journal of the American Helicopter Society*, 17(1):41–48, January 1972.

[17] Johnson, W. Comparison of Calculated and Measured Helicopter Rotor Lateral Flapping Angles. *Journal of the American Helicopter Society*, 26(2):46–50, April 1981.

[18] Riccardi, F. *Model Identification and Control of Variable Pitch Quadrotor UAVs.* PhD thesis, Politecnico di Milano, 2015.

[19] Riccardi, F., Haydar, M. F., Formentin, S. and Lovera, M. Control of variable-pitch quadrotors. In *19th IFAC Symposium on Automatic Control in Aerospace, Würzburg, Germany*, pages 206–211, 2013.